DOI: 10.26599/FSHW.2026.9251123

Contents lists available at SciOpen

Food Science and Human Wellness

journal homepage: https://www.sciopen.com/journal/2097-0765

China Food Publishing Co.

Oral supplementation of TMAO Promotes Vascular Calcification in db/db Mice by Regulating the SIRT1/NF-κB p65/NLRP3 Signaling Axis and the Intestinal Microbiota

Lili Huang[1], Wenjing Wu[2,3,4], Tianmai He[1], Kuiyu Chen[1], Jing Wang[1], Shiqin Xie[5], Huimeng Li[1], Yanyue Yao[1], Zhoujin Tan[6,7]*, Xiaoqin Wang[2,3,4]*

[1] *School of Traditional Chinese Medicine, Hubei University of Chinese Medicine, Wuhan, Hubei, China*

[2] *Department of Nephrology, Affiliated Hospital of Hubei University of Chinese Medicine, Hubei Provincial Hospital of Traditional Chinese Medicine; Wuhan, Hubei, China*

[3] *The First Clinical Medical School, Hubei University of Chinese Medicine; Wuhan, Hubei, China*

[4] *Hubei Key Laboratory of theory and application research of liver and kidney in Traditional Chinese Medicine, Wuhan, Hubei, China*

[5] *School of Public Health, Chongqing Health College, Chongqing, China*

[6] *School of Traditional Chinese Medicine, Hunan University of Chinese Medicine, Changsha, China*

[7] *Hunan Key Laboratory of Traditional Chinese Medicine Prescription and Syndromes Translational Medicine, Changsha, China*

ABSTRACT: This study aimed to investigate the effects of Trimethylamine N-oxide (TMAO) on vascular calcification in db/db mice induced by a high-phosphorus diet and to identify the associated molecular pathways. To establish a VC model, db/db mice were fed a 0.2 % adenine-supplemented high-phosphorus diet, with TMAO and its inhibitor 3,3-dimethyl-1-butanol (DMB) administered via drinking water. The effect of TMAO on renal pathology and colonic mucosal barrier function in db/db mice was evaluated. Micro-computed Tomography(Micro-CT) and Von Kossa staining were used to evaluate the degree of aortic calcification. Western blotting, immunohistochemistry, immunofluorescence, and RT-qPCR were employed to detect the proteins and mRNAs related to the SIRT1/NF-κB p65/NLRP3 signalling pathway. Sequencing of the 16S rRNA gene was performed to analyse changes in the gut microbiota. We found that the serum TMAO level in db/db vascular calcification model mice was significantly elevated, accompanied by calcium and phosphorus metabolism disorders and gut microbiota imbalance, mainly manifested as an increase in the abundance of *Prevotella* and *Desulfovibrio*. TMAO aggravated renal dysfunction and intestinal barrier injury in db/db vascular calcification mice and induced a certain degree of inflammatory response. Moreover, TMAO intervention significantly upregulated the expression of osteogenic marker proteins. In contrast, inhibition of TMAO production by DMB significantly reduced vascular calcification. Mechanistically, TMAO inhibited the activity of the SIRT1 deacetylase, promoted the acetylation of NF-κB p65, and subsequently activated its downstream NLRP3 inflammasome and IL-1β signalling.

Keywords: Diabetic kidney disease; Vascular calcification; Gut microbiota; TMAO; SIRT1; NLRP3 inflammasome

1. Introduction

Diabetic kidney disease (DKD) is a prevalent microvascular complication of diabetes and the leading cause of end-stage renal disease (ESRD). According to the 2019 *Annual Scientific Report on Kidney Diseases*

***Corresponding author**
tanzhjin@sohu.com; wangxiaoqin@hbhtcm.com

Received 21 January 2026
Received in revised from 28 February 2026
Accepted 13 April 2026

in China, DKD has become the leading cause of hospitalization for patients with chronic kidney disease (CKD), accounting for 27 %. The escalating prevalence, mortality, and healthcare costs associated with DKD impose a substantial burden on patients' physical and psychological well-being [1-3]. Furthermore, the progression of DKD, characterized by renal function decline and tubular injury, is frequently accompanied by disorders in calcium-phosphate metabolism, resulting in hyperphosphatemia [4], which drives vascular calcification(VC), a common finding in over 50% of patients with stage 3-5 CKD [5]. As an independent predictor of cardiovascular and all-cause mortality in CKD/ESRD, VC contributes significantly to the 1.36 million annual deaths from CKD-related cardiovascular diseases [6,7]. Thus, exploring novel therapeutic targets against VC in DKD, particularly for early intervention, is an urgent research focus.

Trimethylamine N-oxide (TMAO), a metabolite derived from the gut microbiota, has garnered significant attention in recent years. Its precursor substances, such as choline and carnitine, are mainly derived from the diet—particularly from red meat, eggs, and high-fat dairy products [8]. Gut microbiota utilize the produced trimethylamine (TMA) lyase enzyme complexes, CutC/D, CntA/B, and YeaW/X, to convert these precursors into TMA[9]. Subsequently, TMA is oxidized to TMAO by hepatic flavin-containing monooxygenase 3 (FMO3), enters the circulation, and is ultimately excreted unchanged form in the urine by the kidneys[10,11]. Therefore, during the progression of DKD, disturbances in calcium-phosphate metabolism may serve as an initial trigger for gut microbiota imbalance. Under such conditions, the enrichment of TMA-producing bacteria can enhance TMA production, which is subsequently converted to TMAO in the liver. Due to declining renal function, TMAO accumulates in the body, leading to the release of pro-inflammatory factors into the blood by damaging the intestinal mucosal barrier, thereby establishing a vicious cycle involving renal dysfunction, TMAO retention, and gut microbiota dysbiosis[12].

Nowadays there is growing evidence suggesting an association between TMAO and VC in CKD. However, the underlying molecular mechanisms have not yet been fully understood. Silent information regulator 2-related enzyme 1 (SIRT1), an NAD^+-dependent deacetylase, is a core regulator of energy metabolism, oxidative stress, inflammation, and autophagy [13]. SIRT1 has been confirmed to be closely involved in VC [14,15]. Reduced SIRT1 activity affects downstream targets, such as NF-κB, PGC-1α and FOXOs, leading to excessive activation of inflammatory pathways, mitochondrial dysfunction, and a decline in antioxidant capacity, which jointly promote the occurrence and development of VC [16,17]. It is worth noting that VC is now regarded as a pathological remodeling process driven by inflammation and actively mediated by cells, which is similar to bone formation [18]. However, whether TMAO participates in VC by regulating SIRT1 still needs to be further elucidated.

Based on these findings, we hypothesized that gut microbiota dysbiosis elevates TMAO levels, which in turn promotes VC in DKD by suppressing SIRT1-mediated inflammatory regulation. Our findings are expected to provide new evidence for the prevention and treatment of DKD-related vascular calcification (DKD-VC), thereby contributing to the development of microbiota-targeted strategies for the prevention and treatment of DKD-associated vascular complications.

2. Materials and Methods

2.1. Animals

A total of six 8-week-old male db/m mice and twenty four 8-week-old male db/db mice were used in this study. After one week of adaptive feeding, db/db mice were randomly divided into the db/db-Control, db/db-Model, db/db-TMAO, and db/db-DMB groups (n = 6 per group). All experimental animals were obtained from Hangzhou Ziyuan Experimental Animal Technology Co., Ltd. [License Number: SCXK (Zhejiang) 2024-0004]. The mice were housed in a barrier facility at the Food and Drug Safety Evaluation Centre of Hubei Province (Ethics Approval No. 202410332). The facility was maintained at 23–25 °C, 47–53% humidity, and a 12-h light/dark cycle.

2.2. Grouping and model establishment

DKD was considered successfully established based on the following criteria: (1) consecutive fasting venous blood glucose ≥16.7 mmol/L in db/db mice, (2) urine output >150% of that in db/m mice, and (3) persistent albuminuria. Then, mice in the db/m and db/db-Control groups were given normal chow. Meanwhile, mice in the db/db-Model, db/db-TMAO, and db/db-DMB groups were fed a high-phosphorus diet (1.8% phosphorus, 65% carbohydrate, 10.3% fat, and 24.2% protein; customized from Tianjin Ke'ao Co., Ltd.) combined with 0.2% adenine for 12 weeks to induce vascular calcification. From the fourth week onwards, mice in the db/db-TMAO and db/db-DMB groups were provided with sterile drinking water containing 1% TMAO (53330ES90, Yeasen) and 1% 3,3-dimethyl-1-butanol (DMB; 210-872-6, Aladdin), respectively, for eight consecutive weeks until the end of the experiment.

2.3. General behavioral observations

The general conditions of the mice, such as their mental state and hair color, were observed and recorded at fixed times every day. In addition, body weight and food intake were measured biweekly, and random blood glucose (RBG) levels were assessed monthly.

2.4. Determination of serum biochemical and renal function concentrations

After the experiment, mice were slowly anesthetized by inhalation of 0.2% isoflurane (R510-22-16, RWD Life Science Co., Ltd.). Once anesthesia was confirmed, blood was collected from the orbital sinus, and serum was obtained. After serum collection was completed, the mice were rapidly sacrificed by cervical dislocation. Samples were centrifuged at 13,000 rpm for 15 min and the upper serum was collected. Serum calcium (C004-2-1, Nanjing Jiancheng), phosphorus (C006-1-1, Nanjing Jiancheng), and serum creatinine (SCr, C011-2-1, Nanjing Jiancheng) were analyzed using enzymatic assays. Levels of IL-18 (Cat. No. EK218EGA) and IL-1β (Cat. No. EK201BEGA) were measured using enzyme-linked immunosorbent assay (ELISA) kits (ELK Biotechnology). Microalbumin and urinary creatinine (UCr) concentrations were quantified using an ELISA kit (E-EL-M0792, Elabscience) and a biochemical reagent kit (C011-2-1, Nanjing Jiancheng), respectively. RBG was measured with a blood glucose meter (Freestyle Freedom Lite, Abbott, UK).

2.5. *Ultra-high performance liquid chromatography–tandem mass spectrometry (UHPLC–MS/MS)*

Following blood collection in EDTA tubes, samples were gently inverted and immediately centrifuged at 3,000 rpm for 10 min at 4 °C to obtain plasma. A 50 μL aliquot of plasma was then protein-precipitated with 150 μL of methanol. After vortexing for 1 minute and centrifuging at 13,000 rpm for 10 min (radius: 3 cm), the supernatant was collected for UHPLC–MS/MS analysis. Chromatographic separation was achieved on an X Bridge BEH Amide column (100 × 2.1 mm, 2.5 μm) using mobile phase A, 10 mmol/L ammonium formate (pH 3.5); mobile phase B, acetonitrile. Mass spectrometry was conducted under the following conditions: gas temperature: 350 °C, gas flow: 9 L/min; nebulizer pressure: 2.758×10^5 kPa; sheath gas heater: 300 °C; sheath gas flow: 11 L/min; and capillary voltage: 3,500 V.

2.6. H&E, PAS, and Masson staining

Renal and colon sections were fixed in 4% paraformaldehyde, dehydrated, and embedded in paraffin before being sectioned into 3-μm slices. After dewaxing and hydration, for H&E staining, sections were stained with hematoxylin for 2 min, differentiated with 3% glacial acetic acid, stained with eosin for 2 min, and rinsed with running water. For PAS staining, sections were oxidized with periodic acid for 10 min, rinsed with running water, treated with Schiff's reagent, and incubated in the dark for 10–15 min. Sections were then counterstained with hematoxylin. For Masson staining, sections were first counterstained with hematoxylin to stain nuclei blue, then stained with Masson's trichrome and bright green, respectively, and finally differentiated with absolute ethanol.

2.7. Western blotting

Total protein was extracted using RIPA buffer (P0013B; Beyotime) containing (8242T, HuaBIO), protease inhibitors (Sigma-Aldrich), and protein concentration was determined using a bicinchoninic acid assay kit (P0009, Beyotime Biotechnology). Subsequently, proteins were separated by 10–12% SDS-PAGE, transferred to a polyvinylidene difluoride (PVDF) membrane (IPFL00010, Millipore), and blocked with 5% non-fat milk. Membranes were incubated overnight at 4 °C with primary antibodies against ALP (CY5421, Abways), BMP2 (ab214821, Abcam), occludin (27260-1-AP, Proteintech), claudin-1 (13050-1-AP, Proteintech), OC (16157-1-AP, Proteintech), SIRT1 (16161-1-AP, Proteintech), NF-κB p65 (8242T, HuaBIO), Acetylated p65 (K310, 12629T, Cell Signaling), NLRP3 (WL02635, WanleiBIO), IL-1β (AF4006, Affinity), and β-actin (66009-1-Ig, Proteintech). The next day, membranes were washed with TBST and incubated with HRP-linked anti-rabbit IgG (RGAR001, Proteintech) or HRP-linked anti-mouse IgG (RGAM001, Proteintech). Finally, membranes were visualized using enhanced chemiluminescence reagent (180-506, Tanon, China). Band intensity was quantified using Image Lab (Bio-Rad, Hercules, CA, USA).

2.8. Reverse transcription-quantitative polymerase chain reaction (RT-qPCR)

Total RNA was extracted from aortic tissues with Trizol reagent (R1200, CWBIO), followed by genomic DNA removal and reverse transcription. Relative mRNA expression levels were quantified by real-time PCR using SuperStar Universal SYBR Master Mix (CW3360,CWBIO), with GAPDH as the endogenous control. Data were analyzed using the 2^−ΔΔCT method, and primer sequences are provided in Table S1.

2.9. Immunohistochemistry (IHC) staining

Immunohistochemistry was used to evaluate the expression of aortic SIRT1 and intestinal tight junction proteins occludin and claudin-1. After dewaxing and hydration, endogenous peroxidase activity was quenched and antigen retrieval was performed using microwave heating. Sections were incubated with primary antibodies (as in Western blotting) and secondary antibodies (anti-rabbit EnVision+ System-HRP Labelled Polymer, K4003, DAKO), developed with DAB (045-22833; FujiFilm Wako Pure Chemical Corp.,), and finally examined under a microscope. The average optical density (AOD) of the intestinal sections was measured using ImageJ.

2.10. Immunofluorescence (IF) staining

Aortic sections were fixed in 4% paraformaldehyde (PFA), permeabilized with 0.5% Triton X-100, and blocked with 3% goat serum, then incubated with rabbit anti-SIRT1 primary antibody (16161-1-AP, Proteintech) overnight at 4 °C. The next day, after washing, an Alexa Fluor 488-conjugated goat anti-rabbit IgG antibody was applied. Nuclei were stained with DAPI, and slides were mounted with anti-fade mounting medium. Images were visualized and captured using a microscope.

2.11. Micro-computed Tomography(Micro-CT) imaging of aortic calcification

Micro-CT was used to assess the extent of aortic ring calcification. After cervical dislocation, aortas were harvested and promptly fixed in 4% formaldehyde. Excess fixative was removed with gauze, and samples were scanned using a micro-CT scanner (VNC-102; Pingsheng Medical Technology). Images were reconstructed using Recon software, and the region of interest (ROI) was analyzed using Avatar software. The same ROI was selected for all samples, and parameter values were exported for subsequent analysis.

2.12. Von Kossa staining of the thoracic aorta

After paraffin embedding, sectioning, and dewaxing, thoracic aorta sections were immersed in 2% silver nitrate solution, exposed to ultraviolet light for 30 min, and then treated with 5% sodium thiosulfate solution for 1 min. Counterstaining was performed using eosin. Following dehydration through a graded alcohol series, xylene clearing, and mounting with neutral resin, calcium salt deposition was examined by light microscopy.

2.13. Preparation of total DNA and 16S rRNA high-throughput sequencing

The total genomic DNA was extracted using the Soil DNA Kit (M5635-02, OMEGA). DNA quantity and quality were assessed by spectrophotometry (NanoDrop NC2000, Thermo Fisher Scientific) and agarose gel electrophoresis. The forward primer 27F (5′-ACTCCTACGGGAGGCAGCA-3′) and reverse primer 1492R (5′-GGACTACHVGGGTWTCTAAT-3′) were used for PCR amplification of the bacterial 16S rRNA gene. PCR conditions were as follows: 95 °C for 3 min; 25 cycles of 95 °C for 30 s, 56 °C for 30 s, and 72 °C for 60 s; and a final extension at 72 °C for 5 min. PCR amplicons were purified using Agencourt AMPure Beads (Beckman Coulter, Indianapolis, IN, USA) and then quantified by the PicoGreen dsDNA Assay Kit (Invitrogen, Carlsbad, CA, USA). Sequencing was completed by Paiseno Biological Co., Ltd. (Shanghai, China).

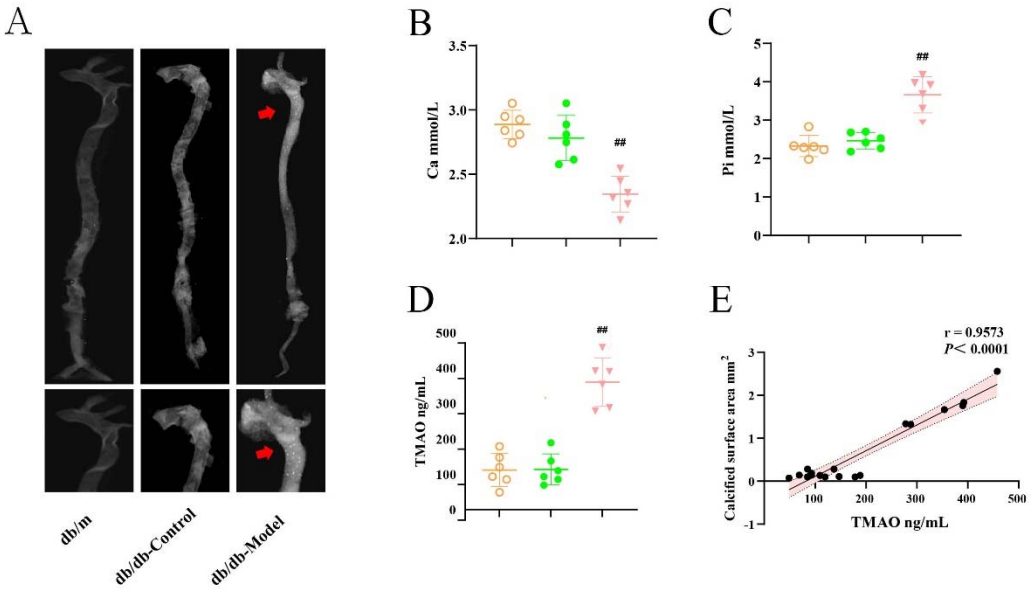
2.14. Statistical analysis

Statistical analysis was performed using SPSS 20.0 and GraphPad Prism 6.0. Continuous data that conformed to a normal distribution are presented as mean ± standard deviation. Independent-samples *t* tests were used for between-group comparisons when data met the assumptions of normality and homogeneity of variance. For multiple comparisons, particularly in the analysis of gut microbiota composition and correlation matrices, the false discovery rate (FDR) approach was applied to correct for Type I errors, with a adjusted p-values < 0.05 considered statistically significant. Statistical analyses included one-way ANOVA for multiple-group comparisons and Pearson correlation for assessing linear relationships between two variables, with a significance level of $\alpha = 0.05$. A $P < 0.05$ was considered statistically significant, and $P < 0.01$ indicated high statistical significance.

3. Results

3.1 Differential level of TMAO, calcium and phosphorus metabolism-related indicators between VC model and normal mice

As shown in Fig. 1A, no apparent calcification was observed in the aortas of db/m and db/db-Control mice. Following administration of adenine combined with a high-phosphorus diet, scattered high-density areas indicative of calcified lesions were observed in the aortic arch of db/db-Model mice. This confirms the successful induction of VC in this model. Subsequently, we measured serum levels of calcium (Ca), phosphorus (Pi), and TMAO in each group. As shown in Fig. 1B–D, mice in the db/db-Model group exhibited significantly lower serum Ca levels ($P < 0.01$) and markedly higher Pi levels ($P < 0.01$) compared to db/m and db/db-Control groups. Notably, serum TMAO concentrations were also significantly elevated in the db/db-Model group ($P < 0.01$), and subsequent correlation analysis revealed a positive association between TMAO levels and the degree of VC. These findings suggest that db/db-VC mice present with markedly increased circulating TMAO levels, accompanied by disturbances in calcium and phosphorus metabolism.



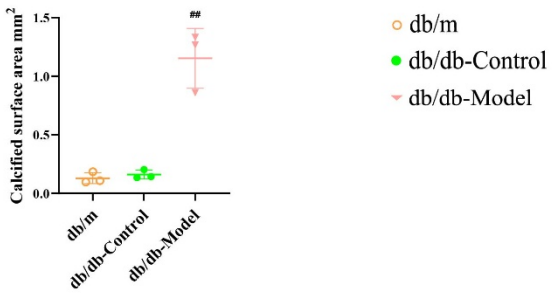


FIG 1. Effects of high-phosphorus diet modeling on VC and serum calcium and phosphorus metabolism-related indicators in db/db mice. (A)Micro-CT and calcification area, n = 3; (B) Ca level; (C) Pi level; (D) TMAO concentrations; (E) correlation analysis between serum TMAO and calcification area. Data are expressed as mean ± SD, n = 6. Compared with the db/db-Control group, # represents $P < 0.05$ and ## represents $P < 0.01$ in the db/db Model group.

3.2. The effects of TMAO on the general condition, renal pathology, and renal function-related indicators of db/db mice

A schematic representation of the animal experiment is shown in Fig. 2A. Firstly, the mice were fed a high-phosphorus diet containing 0.2% adenine and 1.8% phosphorus to induce VC, followed by an 8-week intervention with TMAO. The results suggested that after TMAO intervention, the body weight and random blood glucose(RBG) of mice showed similar trends: both increased during the first 4 weeks and then gradually decreased to a stable level. In addition, food intake, body weight, and RBG showed slightly lower values in the db/db-TMAO group than in the db/db-Model group, but these differences were not statistically significant (Fig. 2B-D). Fig. 2E–G shows the renal function indicators in each group. Compared with the db/db-Control group, serum creatinine, blood urea nitrogen, and the urine microalbumin-to-creatinine ratio were significantly increased in the db/db-Model group ($P < 0.05$ or $P < 0.01$). These indicators were also slightly higher in the db/db-TMAO group than in the db/db-Model group ($P < 0.05$ or not significant).

Moreover, as shown in Fig. 2H, in the db/m group, renal tubules had uniform lumens, and no inflammatory cell infiltration was observed in the renal interstitium. Mice in the db/db-Control group showed localized renal tissue disorganization and mild mesangial proliferation. In contrast, in the db/db-Model group, the glomerular basement membrane was thickened, foot processes were fused, and capillary lumens and Bowman's space were narrowed. After TMAO intervention, Bowman's space appeared enlarged, the mesangial area was widened, and inflammatory cell infiltration and vacuolar degeneration of tubular epithelial cells were observed. Mesangial cell and matrix proliferation were also evident, suggesting that TMAO further aggravated renal structural injury in high-phosphorus-treated db/db mice.

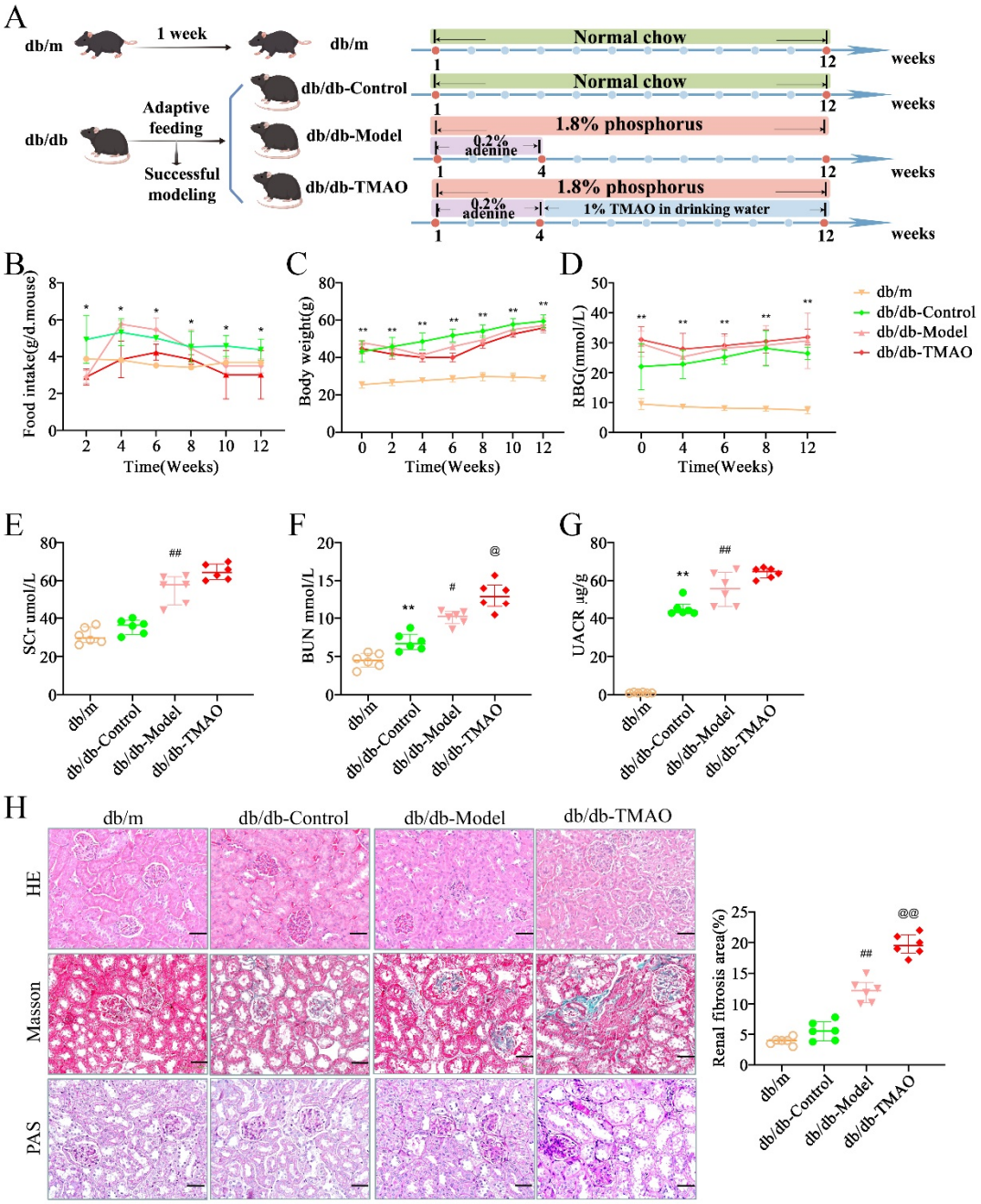


FIG 2 General behavior, renal function, and histology of mice in each group. (A) Animal experimental procedure. (B) Food intake. (C) Body weight. (D) RBG. (E) SCr level. (F) BUN level. (G) UACR level. (H) Renal pathology (H&E, PAS, and Masson staining) and Masson semiquantification(×200). Data are presented as mean ± SD, n = 6. db/m vs. db/db-Control group, * indicates $P < 0.05$ and ** indicates $P < 0.01$. db/db-Control group vs. db/db-Model group, # indicates $P < 0.05$ and ## indicates $P < 0.01$. db/db-Model group vs. db/db-TMAO group, @ indicates $P < 0.05$ and @@ indicates $P < 0.01$.

3.3. Effects of TMAO on gut microbiota diversity in high-phosphorus-treated db/db mice

We employed 16S rRNA sequencing to analyze alterations in the gut microbiota of mice. As shown in Fig. 3A, 460 ASVs were shared among the four groups. The numbers of unique ASVs in the db/m, db/db-Control, db/db-Model, and db/db-TMAO groups were 1690, 2160, 5005, and 3625, respectively, indicating that the microbial community in gut contents changed after TMAO intervention. A gradient stacked area chart comparing taxonomic composition across classification levels (Fig. 3B) showed that TMAO intervention altered gut microbiota composition at six taxonomic levels.

Alpha diversity analysis evaluates the richness and diversity of microbial communities within individual samples. The Chao1 and Observed indices were used to assess richness, whereas the Shannon and PD_whole_tree indices were used to assess diversity and evenness. In this study, the Chao1, PD_whole_tree, Shannon, and Observed indices in the db/db-Model group were increased compared with those in the db/m and db/db-Control groups, and these indices were reduced in the db/db-TMAO group (Fig. 3C–F). These results suggest that in DKD-VC, gut microbiota richness and diversity may be partially reduced by TMAO.

Beta diversity analyses, including NMDS and PCoA, were performed to compare between-group differences in ASV profiles. In NMDS and PCoA, samples from the db/m and db/db-Control groups clustered, whereas samples from the db/db-TMAO group were distinctly separated and more dispersed (Fig. 3G–H). These findings indicate a disrupted gut microbial community structure in DKD-VC mice and suggest that TMAO contributes to these alterations.

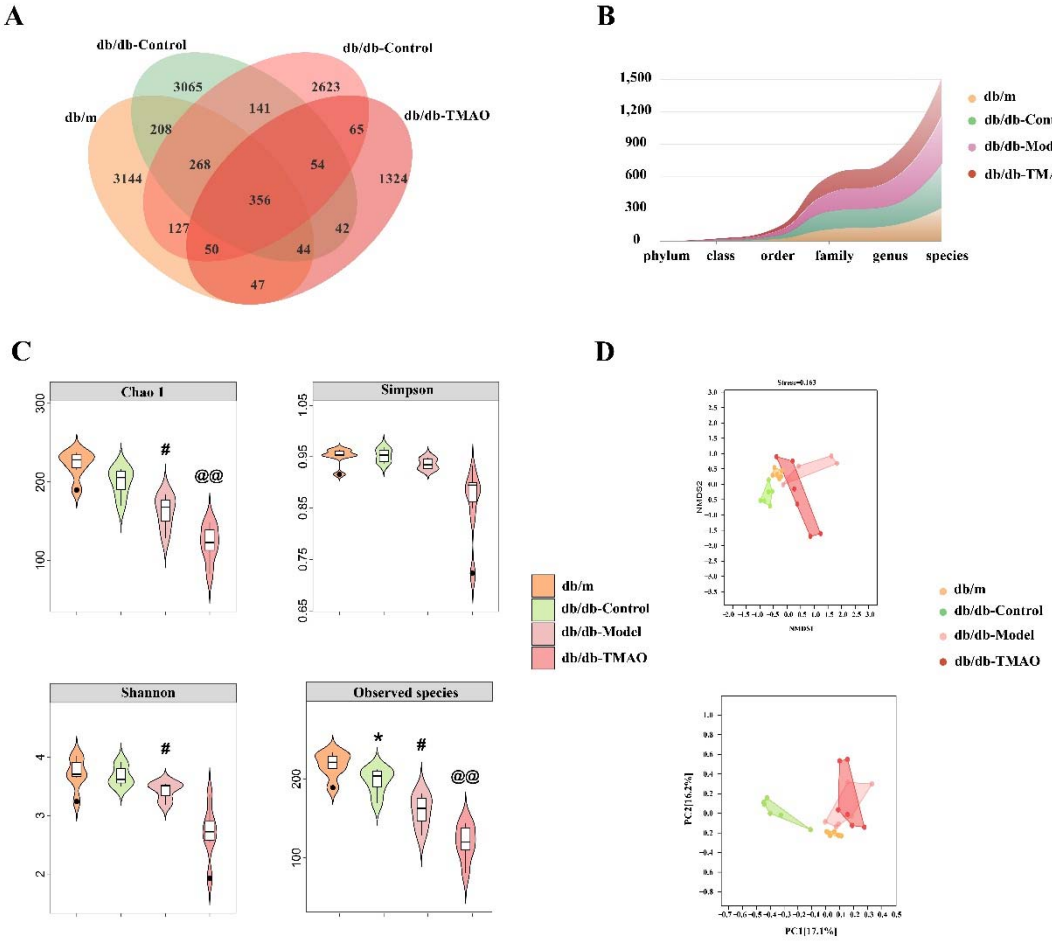


FIG 3. ASV annotation, gene richness, and microbial diversity analysis. (A) ASV classification Venn diagram. (B) Taxonomic composition across six classification levels. (C) Alpha diversity (Chao1, Simpson, Shannon, and Observed indices). (D) Beta diversity (PCoA and NMDS). Data are expressed as mean ± SD, n = 6. db/m vs. db/db-Control group, * indicates $P < 0.05$ and ** indicates $P < 0.01$. db/db-Control group vs. db/db-Model group, # indicates $P < 0.05$ and ## indicates $P < 0.01$. db/db-Model group vs. db/db-TMAO group, @ indicates $P < 0.05$ and @@ indicates $P < 0.01$.

3.4. Changes in gut microbiota composition following TMAO-associated intestinal barrier injury

To evaluate the effects of TMAO on dominant taxa in DKD-VC mice, the relative abundances of the top 10 taxa at each taxonomic level were analyzed. At the phylum level, Actinobacteria, Proteobacteria,

Firmicutes, and Bacteroidetes accounted for the majority of gut contents across all four groups (Fig. 4A). Compared with the other three groups, the relative abundance of Verrucomicrobiota was significantly increased in the db/db-TMAO group ($P < 0.01$) (Fig. 4D).

At the genus level, *Alistipes* A, *Ligilactobacillus*, *Bacteroides* H, *Duncaniella*, and *Prevotella* were dominant genera in all four groups (>1% relative abundance) (Fig. 4B). Statistical analysis showed that, compared with the db/m and db/db-Control group, the relative abundance of *Limosilactobacillus* was significantly increased in the db/db-Model group (Fig. 4E). In addition, *Muribaculum* (Fig. 4F) and *CAG-485* (Fig. 4G) were significantly reduced in the db/db-TMAO group.

At the species level, *Muribaculum gordoncarteri*, *Cryptobacteroides* sp. 900546395, CAG-873 sp. 011959565, *Faecalibaculum rodentium*, and *Bacteroides* H rodentium were dominant species (Fig. 4C). Compared with the db/m group, the relative abundances of *Muribaculum gordoncarteri* and *Faecalibaculum rodentium* in the db/db-TMAO group were significantly decreased (Fig. 4H–I). Together, these results indicate that TMAO intervention altered dominant gut microbiota composition at the phylum, genus, and species levels in DKD-VC mice.

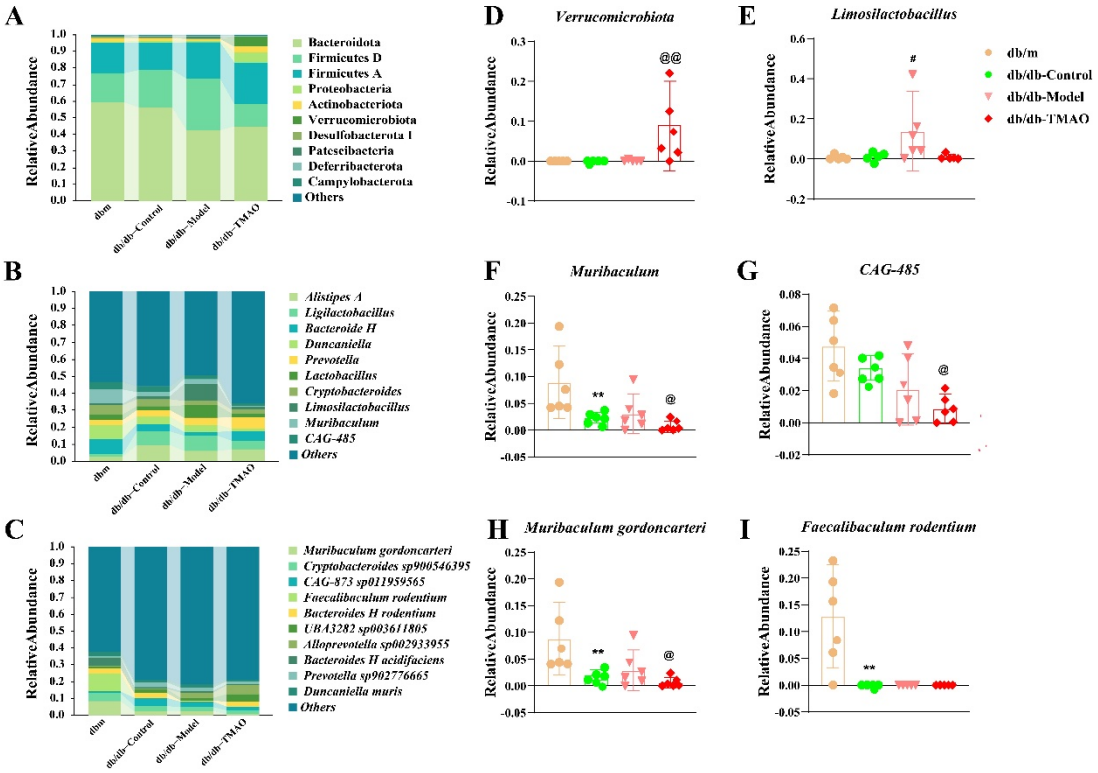


FIG 4. Analysis of dominant taxa in gut contents. (A) Phylum level. (B) Genus level. (C) Species level. (D) Relative abundance of *Verrucomicrobiota*. (E) Relative abundance of *Limosilactobacillus*. (F) Relative abundance of *Muribaculum*. (G) Relative abundance of *CAG-485*. (H) Relative abundance of *Muribaculum gordoncarteri*. (I) Relative abundance of *Faecalibaculum rodentium*. Values are expressed as mean ± SD, n = 6. db/m vs. db/db-Control group, * indicates $P < 0.05$ and ** indicates $P < 0.01$. db/db-Control group vs. db/db-Model group, # indicates $P < 0.05$ and ## indicates $P < 0.01$. db/db-Model group vs. db/db-TMAO group, @ indicates $P < 0.05$ and @@ indicates $P < 0.01$.

3.5. Potential gut microbiota markers associated with TMAO in db/db-VC mice with vascular calcification

In LEfSe analysis, we used a threshold of LDA > 3.5 to identify discriminative taxa. The cladogram (Fig. 5A) and Sankey diagram (Fig. 5B) show taxa with significant differences from the phylum to species levels. In

the db/m group, the characteristic genera were *Bifidobacterium* and *Faecalibaculum*, and the characteristic species included *Bifidobacterium* globosum, *Duncaniella* sp. 001689575, *Muribaculum gordoncarteri*, *Faecalibaculum rodentium*, and *Lactobacillus johnsonii*. In the db/db-Control group, the characteristic genera were 1XD42-69 and *Enterococcus* B, and the characteristic species were *Odoribacter laneus* and 1XD42-69 sp. 003612565. In the db/db-Model group, the characteristic genera were *Limosilactobacillus* and *Prevotella*. In the db/db-TMAO group, the characteristic genera were *Corynebacterium* and *Akkermansia*, and the characteristic species were *Bacteroides* H *caecimuris* and *Akkermansia muciniphila* D.

Compared with the db/m group, the relative abundances of *Muribaculum*, *Duncaniella*, and *Bacteroides* H in the db/db-TMAO group were significantly decreased ($P < 0.001$, $P < 0.01$, and $P < 0.05$, respectively) (Fig. 5C–H). We then performed correlation analyses between selected characteristic genera and UACR, serum Ca, Pi, SCr, BUN, and TMAO. *Duncaniella* was significantly positively correlated with UACR, whereas *Bacteroides* H was positively correlated with UACR, Pi, and SCr. *Muribaculum* was positively correlated with UACR, Pi, SCr, and BUN, and *Corynebacterium* was positively correlated with Ca and BUN (Fig. 5I).

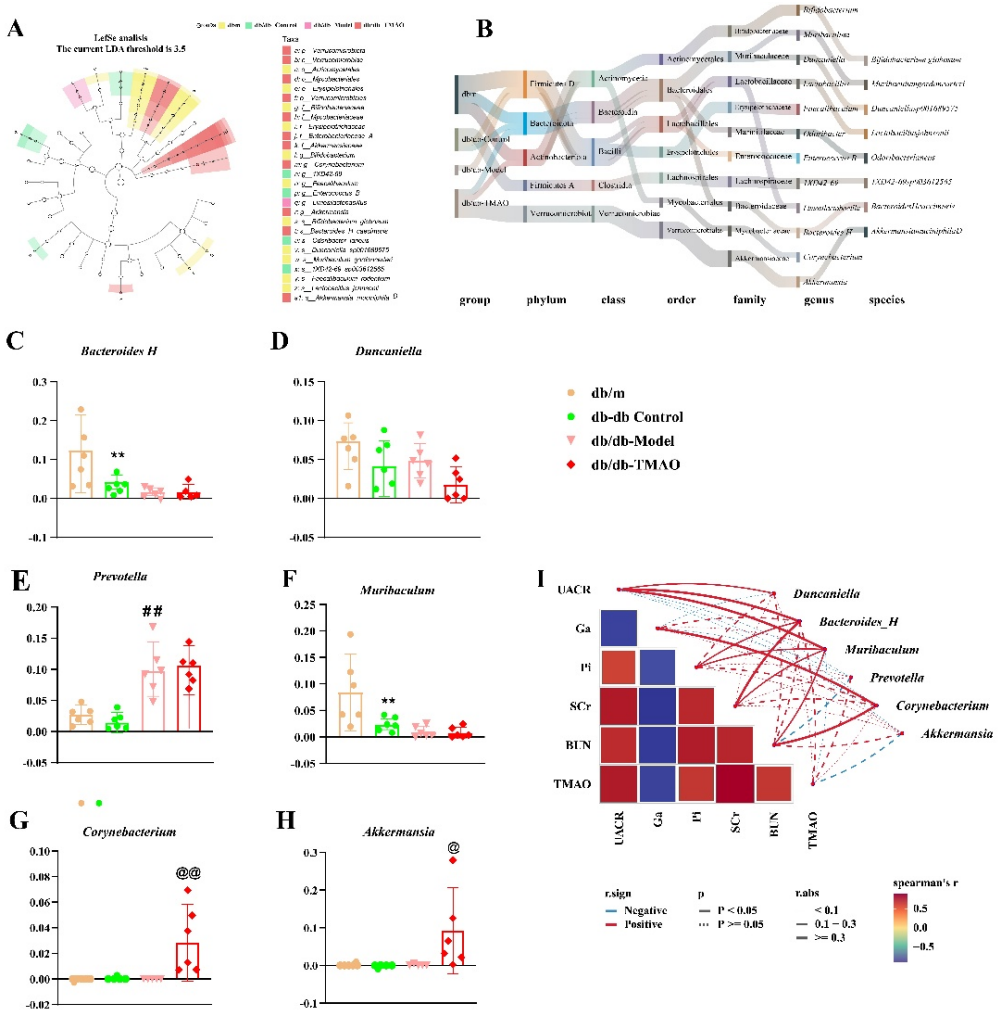


FIG 5. Screening of characteristic microbiota. (A) Cladogram. (B) Sankey diagram. (C–H) Relative abundances of selected genera. (I) Heatmap showing correlations between characteristic taxa, UACR, serum Ca, Pi, SCr, BUN, and TMAO. Red indicates positive correlations and blue indicates negative correlations; color intensity reflects correlation strength. Values are expressed as mean ± SD, n = 6. db/db-Control group vs. db/db-Model group, # indicates $P < 0.05$ and ## indicates $P < 0.01$. db/db-Model group vs. db/db-TMAO group, @ indicates $P < 0.05$ and @@ indicates $P < 0.01$.

3.6. Effects of TMAO on predicted gut microbiota functions in db/db mice with vascular calcification

Functional prediction suggested that gut microbiota functions could be broadly classified into six categories: metabolism, cellular processes, environmental information processing, genetic information processing, human diseases, and organismal systems, with metabolism being the most abundant category (Fig. 6A). Fig. 6B shows the top 10 level-3 metabolic pathways by abundance, indicating that amino acid metabolism, carbohydrate metabolism, metabolism of cofactors and vitamins, and metabolism of terpenoids and polyketides were among the most abundant.

In Fig. 6C, we compared the top 10 KEGG pathways. Compared with the db/db-Control group, the db/db-TMAO group showed decreased abundances of synthesis and degradation of ketone bodies, fatty acid biosynthesis, and pentose and glucuronate interconversions ($P < 0.05$ or $P < 0.01$). In addition, one pathway (pentose and glucuronate interconversions) showed increased abundance in the db/db-TMAO group ($P < 0.05$), as shown in Fig. 6C. Galactose metabolism and the citrate cycle (TCA cycle) also showed an increasing trend in the db/db-TMAO group compared with the other three groups, although the differences were not statistically significant. Overall, these results suggest that VC may be associated with

dysregulated gut microbiota metabolic functions, notably, with alterations in carbohydrate metabolism.

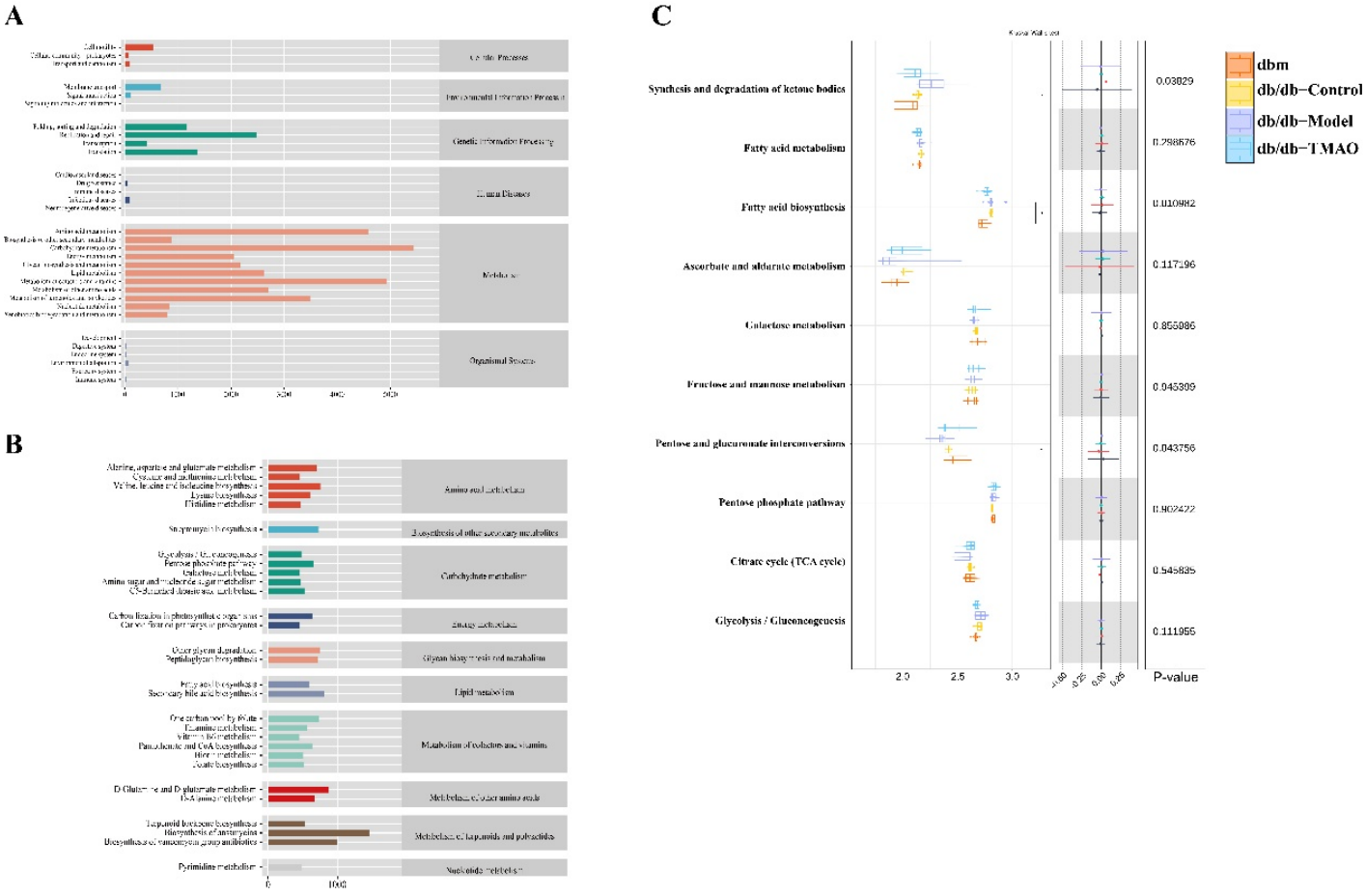
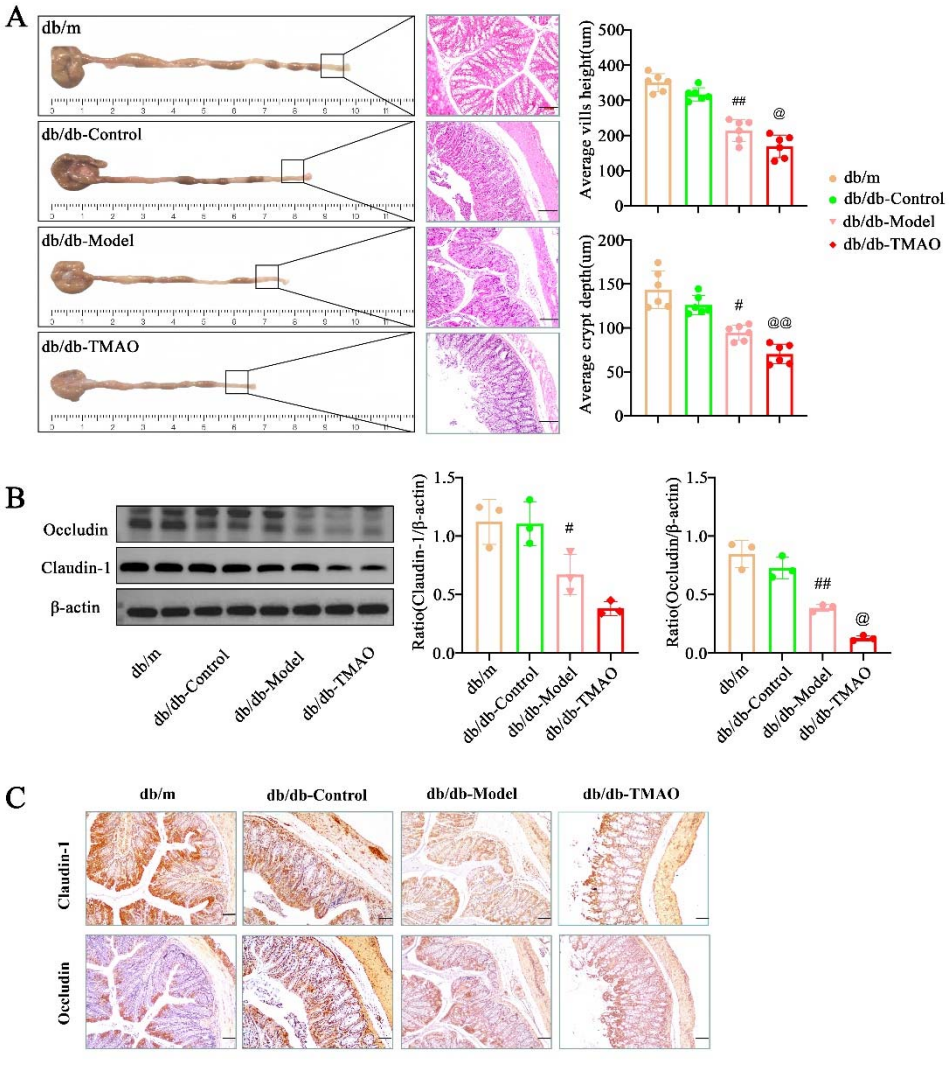


FIG 6. KEGG functional analysis of the gut microbiota. (**A**) Primary metabolic pathways. (**B**) Secondary metabolic pathways. (**C**) Boxplots comparing level-3 metabolic functions between groups. Values are presented as mean ± SD, n = 6. db/db-Control group vs. db/db-Model group, # indicates $P < 0.05$ and ## indicates $P < 0.01$. db/db-Model group vs. db/db-TMAO group, @ indicates $P < 0.05$ and @@ indicates $P < 0.01$.

3.7. TMAO aggravated colonic injury and intestinal barrier disruption in high-phosphorus-treated db/db mice

Given the enrichment of TMA-producing bacteria and the increase in TMAO levels observed in db/db-VC mice, we further investigated the impact of TMAO on intestinal barrier integrity, another key link in the gut-kidney axis. As shown in Fig. 7A, in db/db-TMAO mice, colon length, villus height, and crypt depth were reduced compared with those in db/db-Model mice ($P < 0.01$ or $P < 0.05$). In addition, colonic sections from the db/db-Model group showed inflammatory cell infiltration and disrupted glandular structures. These changes were aggravated by TMAO intervention, with widespread epithelial shedding, necrosis, and loss of mucosal continuity.

Western blotting showed that expression of the tight junction proteins claudin-1 and occludin was significantly reduced in the db/db-Model group (compared with the db/db-Control group, $P < 0.05$ and $P < 0.01$), and further decreased in the db/db-TMAO group (compared with the db/db-Model group, $P > 0.05$ and $P < 0.01$) (Fig. 7B). Immunohistochemistry showed results consistent with Western blotting (Fig. 7C). Together, these findings support the conclusion that TMAO exacerbates intestinal barrier dysfunction induced by high phosphorus in db/db-VC mice, which may be a key upstream link in TMAO activating systemic inflammation and subsequently influencing VC.



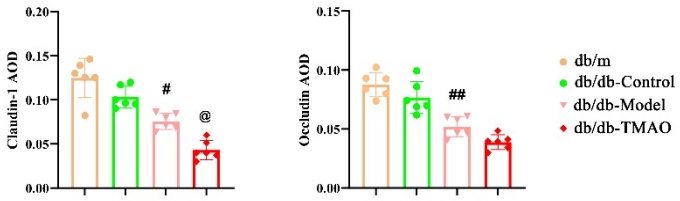
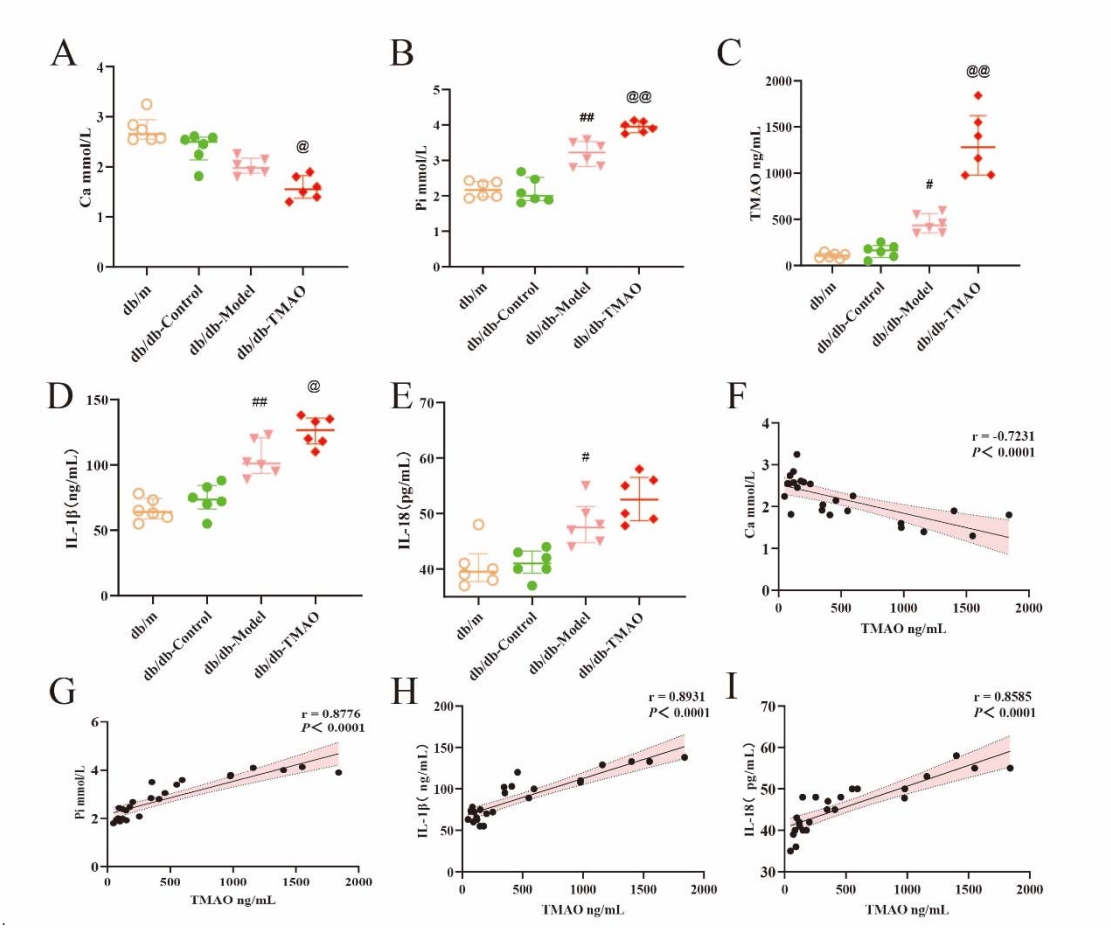


FIG 7 Effects of TMAO on the intestinal barrier in db/db mice induced by a high-phosphorus diet. (A) Macroscopic assessment and H&E staining of the colon (×100). (B) Western blotting and quantification of claudin-1 and occludin. (C) Representative images and quantitative analysis of claudin-1 and occludin expression by immunohistochemistry (×100). Data are expressed as mean ± SD, n = 6. db/db-Control group vs. db/db-Model group, # indicates $P < 0.05$ and ## indicates $P < 0.01$. db/db-Model group vs. db/db-TMAO group, @ indicates $P < 0.05$ and @@ indicates $P < 0.01$.

3.8. TMAO exacerbated calcium–phosphorus metabolic disorder and inflammatory responses induced by high phosphorus in db/db mice

Disorders of calcium–phosphorus metabolism and abnormal inflammatory responses are recognized as key drivers of VC, and the disruption of the intestinal barrier may lead to pro-inflammatory factors entering the circulation, which prompted us to measured relevant serum indicators[19]. The results indicated that, compared with the db/m and db/db-Control groups, Pi, IL-1β, TMAO, and IL-18 levels were significantly elevated in the db/db-Model and db/db-TMAO groups ($P < 0.05$), whereas Ca levels exhibited the opposite trend(Fig. 8A,B,C,D,E). These results suggest that the high-phosphorus modeling induced TMAO accumulation, which in turn triggered a significant inflammatory. Furthermore, correlation analysis revealed that TMAO levels were positively correlated with SCr, BUN, Pi, IL-1β, IL-18, and UACR, and negatively correlated with Ca (Fig. 8F-L).



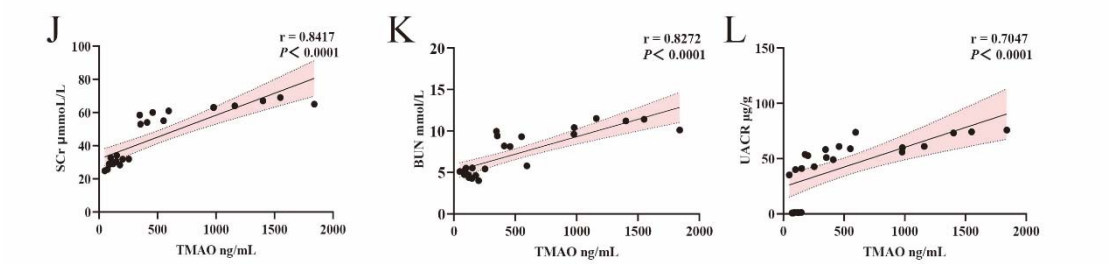


FIG 8 Changes in serum Ca, Pi, TMAO, IL-1β, and IL-18 across groups and correlation analysis. (A) Ca level. (B) Pi level. (C) TMAO level. (D) IL-1β level. (E) IL-18 level. (F–L) Scatter plots showing correlations between TMAO and Ca, Pi, IL-1β, IL-18, SCr, BUN, and UACR. Values are expressed as mean ± SD, n = 6. db/db-Control group vs. db/db-Model group, # indicates $P < 0.05$ and ## indicates $P < 0.01$. db/db-Model group vs. db/db-TMAO group, @ indicates $P < 0.05$ and @@ indicates $P < 0.01$.

3.9. TMAO promotes vascular calcification in db/db mice, and calcification is alleviated by DMB intervention

Previous studies on TMAO in cardiovascular diseases have mainly focused on atherosclerosis [20], whereas its effects on VC remain unclear. Given that we observed the enrichment of TMA-producing bacteria and the increase in blood TMAO levels in mice after high-phosphorus-induced, we therefore examined whether TMAO could promote high-phosphorus–induced VC and compared its effects with those of the TMAO inhibitor DMB (Fig. 9A). Von Kossa staining specifically stains calcium salts (mainly calcium phosphate/hydroxyapatite) brown to black. As shown in Fig. 9B, compared with the db/db-Model group, calcification in the db/db-TMAO group was significantly increased ($P < 0.01$). In contrast, calcification in the db/db-DMB group was significantly reduced ($P < 0.05$). Micro-CT results (Fig. 9C) supported these findings. In the aortic arch and abdominal aorta of mice in the db/db-Model and db/db-TMAO groups, scattered high-density regions were observed. Quantitative analysis further demonstrated that the calcification area was significantly larger in the db/db-TMAO group than in the db/db-Model group ($P < 0.05$; Fig. 9C), whereas DMB intervention reduced calcification.

We then performed Western blotting to assess osteogenic protein expression in aortic tissue. As shown in Fig. 9D–E, levels of ALP, BMP-2, and OC in the db/db-TMAO group were significantly higher than those in the db/db-Model group ($P < 0.01$, $P < 0.05$, and $P < 0.05$, respectively), whereas DMB partially reversed these changes (compared with the db/db-Model group, $P > 0.05$, $P < 0.05$, and $P < 0.01$, respectively). Collectively, these results indicate that TMAO aggravates high-phosphorus-induced aortic calcification in db/db mice and upregulates osteogenic protein expression, whereas inhibition of TMAO production by DMB alleviates VC.

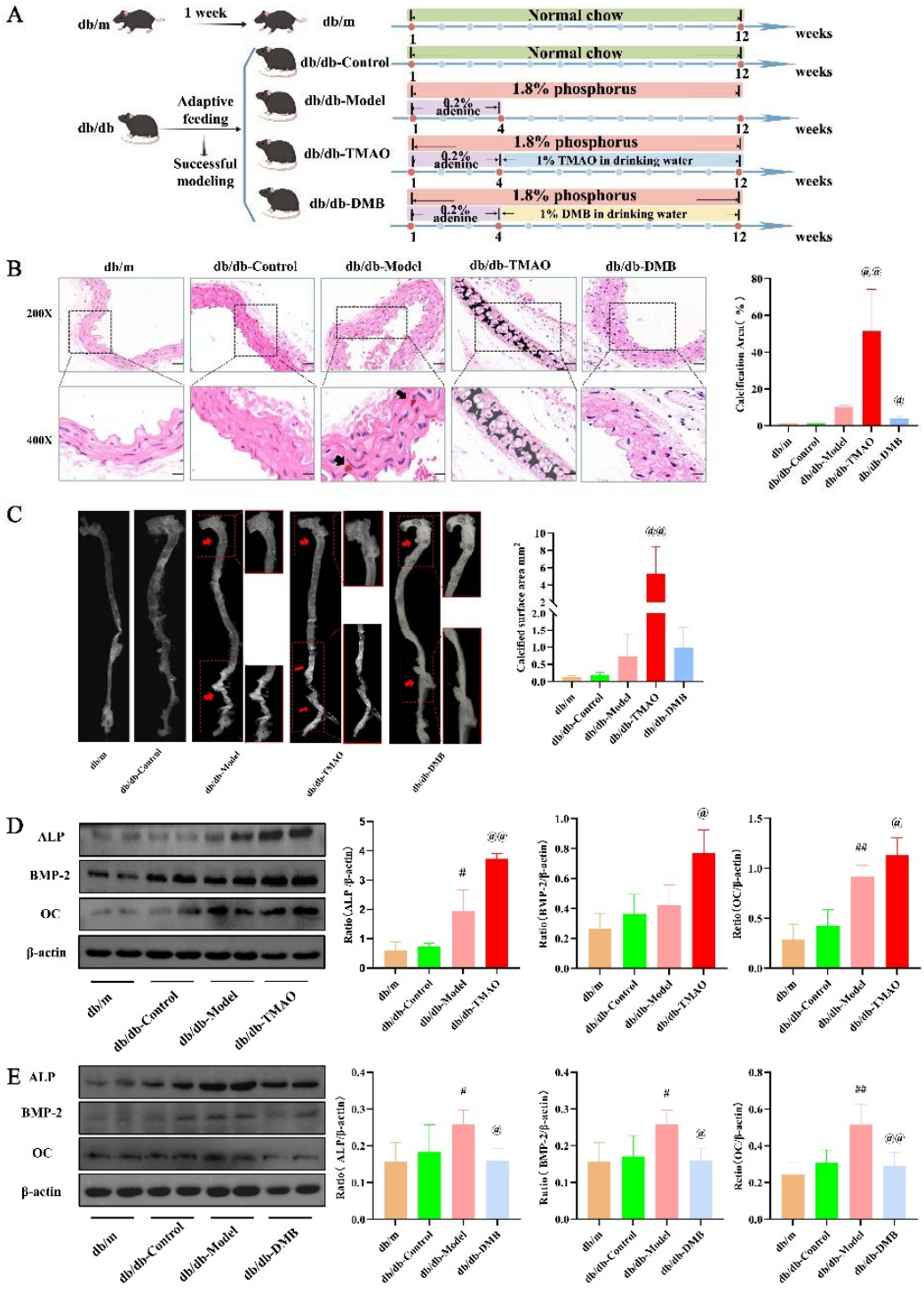


FIG 9 . Effects of TMAO on aortic calcification induced by high phosphorus in db/db mice. (A) Experimental design. (B) Von Kossa staining and statistical analysis of calcified surface area. (C) Micro-CT imaging and quantitative analysis of calcification. (D) Western blotting analysis of osteogenic-related proteins in the aorta following TMAO intervention and quantification analysis. (E) Western blotting analysis of osteogenic-related proteins in the aorta following DMB intervention and quantification analysis. Data are expressed as mean ± SD, n = 6. db/db-Control group vs. db/db-Model group, # indicates $P < 0.05$ and ## indicates $P < 0.01$. db/db-Model group vs. db/db-TMAO group, @ indicates $P < 0.05$ and @@ indicates $P < 0.01$.

3.10. Regulatory effects of TMAO on the SIRT1/NF-κB p65/NLRP3 signaling pathway in the aorta of db/db-VC mice

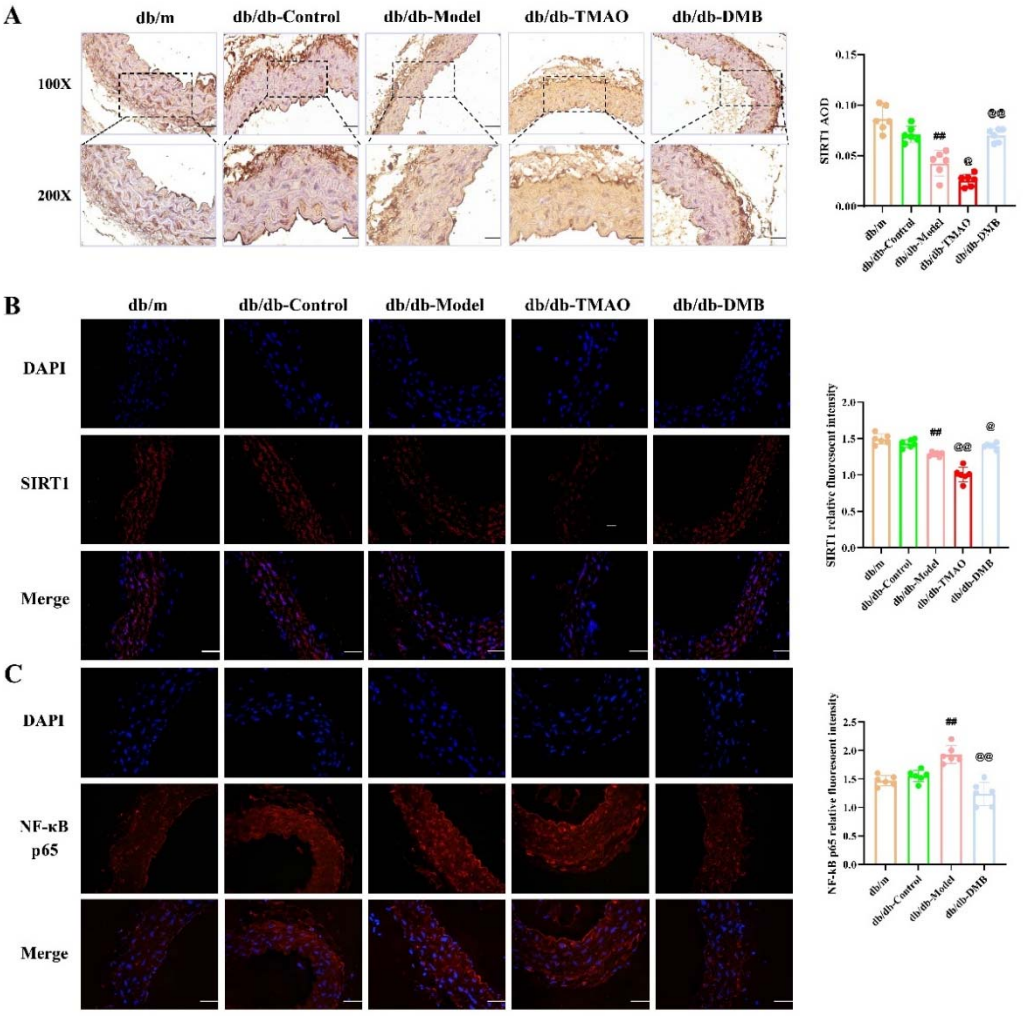
To further clarify the mechanisms by which TMAO regulates VC, we first evaluated SIRT1 protein expression in the aorta using immunohistochemistry and immunofluorescence staining. As shown in Fig.

10A–B, SIRT1 expression was notably reduced in the db/db-TMAO group, while it was significantly increased in the db/db-DMB group. This indicates that the promotion of VC by TMAO may be related to the regulation of SIRT1 expression.

SIRT1, a deacetylase, can deacetylate lysine 310 of the NF-κB p65 subunit, thereby reducing its transcriptional activity and proinflammatory target gene expression [21]. We then detected protein and mRNA levels related to the SIRT1/NF-κB p65/NLRP3 pathway using Western blotting, IFC, and RT-qPCR, respectively.

As illustrated in Fig. 10C–D, compared with the db/db-Model group, SIRT1 expression in the db/db-TMAO group was markedly downregulated, accompanied by increased NLRP3, IL-1β, and the acetylated NF-κB p65/total NF-κB p65 ratio (Ac-p65/p65). Compared with the db/db-Model group, SIRT1 expression further decreased in the db/db-TMAO group, whereas NLRP3, IL-1β, and Ac-p65/p65 were significantly increased. In contrast, inhibition of TMAO reversed the upregulation of NLRP3, IL-1β, and Ac-p65/p65.

Similarly, our RT-qPCR results revealed that TMAO intervention suppressed SIRT1 mRNA levels and upregulated NF-κB p65, NLRP3, IL-1β, and IL-18 expression(Fig. 10G). DMB prevented SIRT1 downregulation, as well as inhibited upregulation of the mRNA of NF-κB p65, NLRP3, and IL-1β (Fig. 10H). These findings suggest that during VC in db/db mice, TMAO may promote calcification by suppressing SIRT1, thereby increasing p65 acetylation and activating downstream inflammatory signaling.



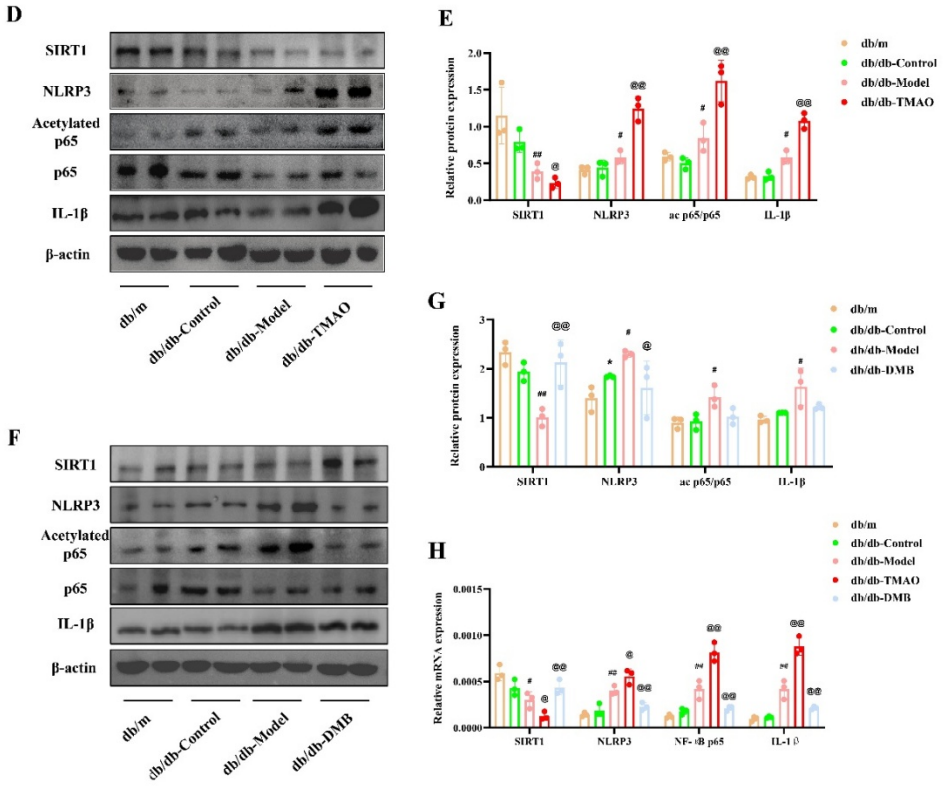


FIG 10 . Regulatory effects of TMAO on the SIRT1/NF-κB p65 signaling pathway in db/db vascular calcification mice. (A) Immunohistochemistry of SIRT1 expression in the aorta. (B) Immunofluorescence staining of SIRT1 in the aorta. (C) Western blotting of proteins related to the SIRT1/NF-κB p65 signaling pathway in the aorta. (D) Quantification of protein expression. (E) RT-qPCR analysis of SIRT1, NLRP3, NF-κB p65, and IL-1β mRNA levels in aortic tissue. Data are expressed as mean ± SD, n = 6. db/m vs. db/db-Control group, * indicates $P < 0.05$ and ** indicates $P < 0.01$. db/db-Control group vs. db/db-Model group, # indicates $P < 0.05$ and ## indicates $P < 0.01$. db/db-Model group vs. db/db-TMAO group, @ indicates $P < 0.05$ and @@ indicates $P < 0.01$.

4. Discussion

The pathological mechanisms underlying VC are intricate, and traditional risk factors alone cannot fully explain its high prevalence. In-depth investigation of the gut microbiota and its metabolites may help explain the bidirectional interactions between the gut and the kidney. This study elucidates the molecular mechanism by which the TMAO-mediated "gut-kidney axis" contributes to VC in DKD. In advanced stages, the overgrowth of uremic toxin-producing microbiota [22] and declining renal function lead to TMAO accumulation, initiating VC. Mechanistically, TMAO increases intestinal mucosal barrier permeability [23], enabling pro-inflammatory mediators to enter the circulation, while its abnormal elevation concurrently exacerbates renal dysfunction and disrupts calcium-phosphorus homeostasis. Collectively, these processes drive the progression of VC.

Our DKD-VC model mice exhibited gut microbiota dysbiosis. db/db-Model group exhibited reduced Bacteroidota and Actinobacteria alongside expansion of Firmicutes, Proteobacteria, and Deferribacterota—phyla known to harbour TMA-producing bacteria [24]. At the genus level, the relative abundances of TMA-producing genera, including *Prevotella* and *Limosilactobacillus*, were significantly enriched in the db/db-Model group. Notably, certain strains within the genus *Limosilactobacillus*, such as *Limosilactobacillus fermentum* LF1143, have been documented to possess TMA-producing capabilities[25]. Moreover, *Prevotella* may disrupt the intestinal barrier via lipopolysaccharide (LPS) production, which can activate NF-κB signaling and promote osteogenic differentiation and

calcification of vascular smooth muscle cells (VSMCs) [26,27]. After TMAO treatment, the relative abundance of the Verrucomicrobiota phylum was significantly increased, whereas the relative abundances of *Duncaniella*, *Muribaculum*, and CAG-485 were reduced. *Corynebacterium* and *Akkermansia* were identified as characteristic genera in the TMAO group. Among these, *Muribaculum* has been reported to alleviate VC by regulating vitamin K2 and matrix Gla protein (MGP) activation [28]. Previous in vivo and in vitro studies have shown that *Corynebacterium* can absorb calcium ions to form crystalline hydroxyapatite, thereby triggering chronic inflammation and fibrosis, and ultimately contributing to calcification [29].

As a key defense against intestinal toxins and pro-inflammatory factors, the intestinal mucosal barrier is essential for maintaining host homeostasis[30]. In our study, TMAO further aggravated intestinal barrier injury. Disruption of the intestinal barrier may facilitate the translocation of pro-inflammatory mediators such as LPS into the bloodstream, triggering systemic inflammation and thereby promoting vascular calcification [31].Yu et al. reported that serum TMAO levels in individuals with early CKD are higher than those in healthy controls [32]. Furthermore, serum TMAO levels are positively correlated with cystatin C, an early marker of renal injury, suggesting that circulating TMAO begins to increase even at the early stage of renal impairment, suggesting that circulating TMAO begins to increase even at the early stage of renal impairment. Consistent with these observations, we found that db/db mice treated with TMAO exhibited more severe renal dysfunction and intestinal mucosal barrier damage. Importantly, barrier dysfunction can further exacerbate dysbiosis by altering the local microenvironment, and certain genera (such as *Prevotella*) may directly impair barrier integrity [33], forming a vicious cycle of "dysbiosis–barrier damage–inflammation" [34]. This cycle places TMAO at the center, where it is both a consequence of initial dysbiosis and a driver of subsequent barrier failure and inflammation.

It is well known that VC is an actively regulated, inflammation-driven pathological process similar to bone formation [35], largely mediated by phenotypic transformation of VSMCs [36]. Our results indicate that TMAO suppresses SIRT1 expression in aortic tissue, thereby promoting NF-κB p65 acetylation and activating the downstream NLRP3 inflammasome, leading to increased production of IL-1β. Previous studies have shown that downregulation of SIRT1 promotes osteogenic transformation of VSMCs and age-related VC [15]. Our findings further suggest that in DKD-VC, TMAO-induced SIRT1 suppression activates the NF-κB p65/NLRP3 pathway and enhances inflammatory signaling in vascular tissue. Persistent low-grade inflammatory signals may promote calcium phosphate crystal deposition in the vascular wall and upregulate osteogenic transcription factors such as Runx2, thereby initiating osteogenic transdifferentiation of VSMCs [37]. Correlation analysis supports this interpretation, as TMAO levels were positively correlated with inflammatory cytokines (IL-1β and IL-18) and Pi and UACR, while negatively correlated with SIRT1 expression. DMB treatment attenuated aortic calcification and reduced osteogenic marker expression. Collectively, these findings suggest that TMAO is an important mediator of DKD-associated VC, and that targeting TMAO generation or its downstream signaling may represent a feasible therapeutic strategy.

5. Conclusion

In conclusion, we demonstrated that under high-phosphorus conditions, TMAO exacerbates VC in db/db mice, and the SIRT1/NF-κB p65/NLRP3 signaling axis plays a key role in this process (Fig. 11). Our findings support a mechanistic link between gut microbiota–derived TMAO and VC in DKD and suggest that targeting gut microbiota and TMAO levels may provide therapeutic opportunities to prevent or treat DKD-associated VC.

Furthermore, our findings have potential clinical translational implications. Future studies could further investigate the associations among dietary patterns (e.g., high choline intake), circulating TMAO levels, and vascular calcification in clinical settings. Moreover, TMAO-lowering strategies—including dietary modification, probiotic intervention to modulate gut microbiota, and targeted inhibition of TMA-producing bacteria—warrant further investigation as potential approaches to reduce cardiovascular complications in high-risk populations with DKD.

However, this study has several limitations. First, as an animal study conducted in db/db mice, our findings require further validation through clinical evidence or in vitro experiments using aortic smooth muscle cell lines to support their translational relevance. Second, additional in vivo studies—such as those employing germ-free mouse models or fecal microbiota transplantation (FMT)—could help further elucidate the causal role of gut microbiota in linking the metabolite TMAO to vascular calcification.

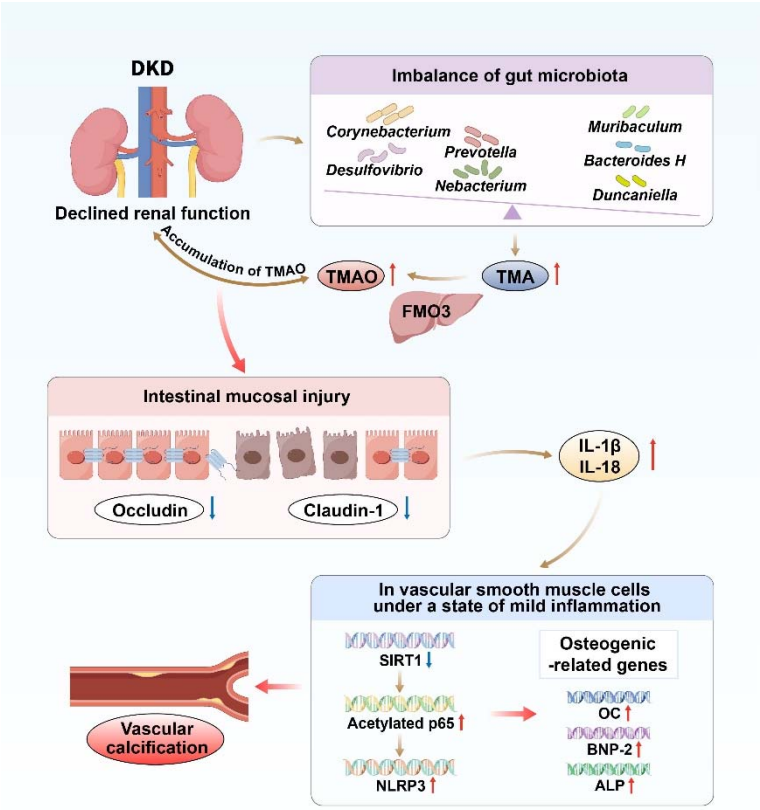


FIG 11. TMAO facilitates VC by influencing the SIRT1/NF-κB p65/NLRP3 signaling pathway.

Ethics Approval

The Animal Ethics and Welfare Committee of the Food and Drug Safety Evaluation Centre of Hubei Province approved the animal experiments, which complied with the animal ethics requirements (Ethics Approval No. 202410332). All methods are reported in accordance with the ARRIVE guidelines

(https://arriveguidelines.org) for the reporting of animal experiments and were carried out adhering to relevant guidelines and regulations. All authors were aware of and approved of this animal experiment.

Funding

Thanks to the National Natural Science Foundation of China (82374384, 82575013)for supporting this research.

Conflict of Interest

The authors declare that there is no conflict of interest regarding the publication of this paper.

Data Availability

The datasets presented in this study can be found in online repositories. The names of the holds/repositories and accession number(s) can be found below: https://www.ncbi.nlm.nih.gov/, PRJNA1298210. They also can be made available from the corresponding author on reasonable request.

References

R.C. Stanton, Diabetic Kidney Disease and Hypertension. Exp. Clin. Endocrinol. Diabetes. 124(2) (2016) 93-98, https://doi.org/10.1055/s-0035-1559760.

M. Maqbool, M.E. Cooper, K.A.M. Jandeleit-Dahm, Cardiovascular Disease and Diabetic Kidney Disease, Semin. Nephrol. 38(3) (2018) 217-232, https://doi.org/10.1016/j.semnephrol.2018.02.003.

M. Lehto, P.H. Groop, The Gut-Kidney Axis: Putative Interconnections Between Gastro intestinal and Renal Disorders, Front. Endocrinol (Lausanne). 9 (2018) 553, https://doi.org/10.3389/fendo.2018.00553

V. Martinez Leon, R. Hilburg, K. Susztak, Mechanisms of diabetic kidney disease and established and emerging treatments, Nat. Rev. Endocrinol. 22 (1) (2026) 21–35, https://doi.org/10.1038/s41574-025-01171-3.

S.S. Martin, A.W. Aday, Z.I. Almarzooq, C.A.M. Anderson, P. Arora, C.L. Avery, C.M. Baker-Smith, B. Barone Gibbs, A.Z. Beaton, A.K. Boehme, Y. Commodore-Mensah, et al. Palaniappan, American Heart Association Council on Epidemiology and Prevention Statistics Committee and Stroke Statistics Subcommittee, Correction to: 2024 Heart Disease and Stroke Statistics: A Report of US and Global Data From the American Heart Association, Circulation. 151 (25) (2025) e1095, https://doi.org/10.1161/CIR.0000000000001344.

GBD Chronic Kidney Disease Collaboration, Global, regional, and national burden of chronic kidney disease, 1990-2017: a systematic analysis for the Global Burden of Disease Study 2017, Lancet. 395 (10225) (2020) 709-733, https://doi.org/10.1016/S0140-6736(20)30045-3.

A. Amaya-Garrido, M. Brunet, B. Buffin-Meyer, A. Piedrafita, L. Grzesiak, E. Agbegbo, A. Del Bello, I. Ferrandiz, S. Ardeleanu, M. Bermudez-Lopez, C. Fedou, M. Camus, O. Burlet-Schiltz, J. Massines, M. Buléon, G. Feuillet, M. Alves, E. Neau, A. Casemayou, B. Breuil, J.S. Saulnier-Blache, C. Denis, J. Voelkl, G. Glorieux, S. Hobson, S. Arefin, A. Rahman, K. Kublickiene, P. Stenvinkel, J.L. Bascands, S. Faguer, J.M. Valdivielso, J.P. Schanstra, J. Klein, Calprotectin is a contributor to and potential therapeutic target for vascular calcification in chronic kidney disease, Sci. Transl. Med. 15 (712) (2023) eabn5939, https://doi.org/10.1126/scitranslmed.abn5939.

Chen Y, Weng Z, Liu Q, Shao W, Guo W, Chen C, Jiao L, Wang Q, Lu Q, Sun H, Gu A, Hu H, Jiang Z. FMO3 and its metabolite TMAO contribute to the formation of gallstones, Biochim Biophys Acta Mol Basis Dis. 1865(10)(2019) :2576-2585, https://doi: 10.1016/j.bbadis.2019.06.016.

Y. Lei, G. Xiong, D. Lei, H. Wu, X. Peng, L. Chen, Q. Fang, Y. Wu, Y. Wu, X. Li, Y. Li, Gut microbiota-derived TMAO drives the kidney-bone-vascular axis in chronic kidney disease complications, Renal Failure. 47 (1) (2025) 2575434, https://doi.org/10.1080/0886022X.2025.2575434.

L. Huang, W. Wu, X. Wang, Analysis of the microecological mechanism of diabetic kidney disease based on the theory of "gut-kidney axis": A systematic review, Open Life Sci. 19 (1) (2024) 20220909, https://doi.org/10.1515/biol-2022-0909.

A. Ramezani, D.S. Raj. The gut microbiome, kidney disease, and targeted interventions, J. Am. Soc. Nephrol. 25 (4) (2014) 657-670, https://doi.org/10.1681/ASN.2013080905.

M. Ribeiro, J.A. Kemp, L. Cardozo, D. Vargas, M. Ribeiro-Alves, P. Stenvinkel, D. Mafra, Trimethylamine N-Oxide (TMAO) Plasma Levels in Patients with Different Stages of Chronic Kidney Disease, Toxins (Basel). 17 (1) (2024) 15, https://doi.org/10.3390/toxins17010015.

Z. Liu, H. Liu, S. Liu, B. Li, Y. Liu, E. Luo, SIRT1 activation promotes bone repair by enhancing the coupling of type H vessel formation and osteogenesis, Cell Proliferation. 57 (6) (2024) e13596, https://doi.org/10.1111/cpr.13596.

G.D.S. Feltran, E.A. Alves Dos Santos, A.F. de Camargo Andrade, W.F. Zambuzzi, R.A,F. da Silva, Epigenetic modulation of vascular calcification: Looking for comprehending the role of sirt1 and histone acetylation in VSMC phenotypic transition, Exp. Cell Res. 443 (1) (2024) 114311, https://doi.org/10.1016/j.yexcr.2024.114311.

Xu J, Kitada M, Koya D. The impact of mitochondrial quality control by Sirtuins on the treatment of type 2 diabetes and diabetic kidney disease, Biochim Biophys Acta Mol Basis Dis. 1866(6)(2020):165756. https://doi: 10.1016/j.bbadis.2020.165756.

Jaikumkao K, Thongnak L, Htun KT, Pengrattanachot N, Phengpol N, Sutthasupha P, Promsan S, Montha N, Sriburee S, Kothan S, Lungkaphin A. Dapagliflozin and metformin in combination ameliorates diabetic nephropathy by suppressing oxidative stress, inflammation, and apoptosis and activating autophagy in diabetic rats, Biochim Biophys Acta Mol Basis Dis. 1870(1)(2024),166912.https:// doi: 10.1016/j.bbadis.2023.166912.

Y. Yin, M. Wei, X. Jiang, M. Liu, X. Shi, X. Zhang, L. Wang, G. Liu, M. Zheng, F. Ma, Gut microbiota-derived trimethylamine-N-oxide inhibits SIRT1 to regulate SM22α-mediated smooth muscle cell inflammation and promote atherosclerosis progression, J. Cell Commun. Signaling. 19 (2) (2025) e70021, https://doi.org/10.1002/ccs3.70021.

P. Libby, The changing landscape of atherosclerosis, Nature. 592 (7855) (2021) 524-533, https://doi.org/10.1038/s41586-021-03392-8.

W.J. Wu , L. Wang, X.Q. Wang. Interpretation of "Kidneys Govern Bones" Theory based on the αKlotho-FGF23-FGFRs Axis, Integr. Med. Nephrol. Androl. 12 (1) (2025) e24-00032, https://doi.org/10.1097/IMNA-D-24-00032.

Y. Huang, H. Zhang, X. Fan, J. Wang, Y. Yin, Y. Zhang, K. Shi, F. Yu. The Role of Gut Microbiota and Trimethylamine N-oxide in Cardiovascular Diseases, J. Cardiovasc Transl. Res. 16 (3) (2023) 581-589, https://doi.org/10.1007/s12265-022-10330-0.

W. Dong, K. Zhang, X. Wang, J. Li, H. Zou, Y. Yuan, J. Gu, J. Zhu, G. Liu, Z. Liu, R. Song, SIRT1 alleviates Cd nephrotoxicity through NF-κB/p65 deacetylation-mediated pyroptosis in rat renal tubular epithelial cells, Sci. Total Environ. 929 (2024) 172392, https://doi.org/10.1016/j.scitotenv.2024.172392.

H.L. Zhao, T.T. Zhao, P. Li, Gut Microbiota-derived Metabolites: A New Perspective of Traditional Chinese Medicine Against Diabetic Kidney Disease, Integr. Med. Nephrol. 11 (2) (2024) e23-00024, https://doi.org/10.3389/fphar.2024.1405928.

L. Fang, J. Shen, N. Xiao, Z. Tan, TMAO Activates the NLRP3 Inflammasome, Disrupts Gut-Kidney Interaction, and Promotes intestinal Inflammation, Int. J. Mol. Sci. 26 (15) (2025) 7441, https://doi.org/10.3390/ijms26157441.

Q.Y. Hao, J. Yan, J.T. Wei, Y.H. Zeng, L.Y. Feng, D.D. Que, S.C. Li, J.B. Guo, Y. Fan, Y.F. Ding, X.L. Zhang, P.Z. Yang, J.W. Gao, Z.H. Li, *Prevotella* copri promotes vascular calcification via lipopolysaccharide through activation of NF-κB signaling pathway, Gut Microbes. 16 (1) (2024) 2351532, https://doi.org/10.1080/19490976.2024.2351532.

S. Song, X. Yu, C. Xie, Z. Li, Y. Zhang, Y. Liu, Z. Qiu, T. Wang, H. Su, H. Huang, P. Luo, Long-Term In Vivo Administration of Panaxynol Alleviates Diabetes-Induced Vascular Calcification by Modulating Sirt6-Mediated sEH Function in Perivascular Adipose Tissue, J. Agric. Food Chem. 73 (29) (2025) 18268–18279, https://doi.org/10.1021/acs.jafc.5c01982.

X. Zhang, Y. Li, P. Yang, X. Liu, L. Lu, Y. Chen, X. Zhong, Z. Li, H. Liu, C. Ou, J. Yan, M. Chen, Trimethylamine-N-Oxide Promotes Vascular Calcification Through Activation of NLRP3 (Nucleotide-Binding Domain, Leucine-Rich-Containing Family, Pyrin Domain-Containing-3) Inflammasome and NF-κB (Nuclear Factor κB) Signals, Arterioscler. Thromb. Vasc. Biol. 40 (3) (2020) 751-765, https://doi.org/10.1161/ATVBAHA.119.313414.

S. Kiechl, G. Schett, J. Schwaiger, K. Seppi, P. Eder, G. Egger, P. Santer, A. Mayr, Q. Xu, J. Willeit, Soluble receptor activator of nuclear factor-kappa B ligand and risk for cardiovascular disease, Circulation. 116 (4) (2007) 385-91, https://doi.org/10.1161/CIRCULATIONAHA.106.686774.

P.X. Yang, C.R. You, Y.H. Lin, C.S. Wang, Y.W. Hsu, T.M. Pan, C.L. Lee, Effects of *Monascus pilosus* SWM 008-Fermented Red Mold Rice and Its Functional Components on Gut Microbiota and Metabolic Health in Rats, Foods. 14 (4) (2025) 651, https://doi.org/10.3390/foods14040651.

Ma L, Zhang L, Li J, Zhang X, Xie Y, Li X, Yang B, Yang H. The potential mechanism of gut microbiota-microbial metabolites-mitochondrial axis in progression of diabetic kidney disease. Mol Med. 2023 Oct 31;29(1):148. doi: 10.1186/s10020-023-00745-z. PMID: 37907885; PMCID: PMC10617243.

YAN S K, YU L L, TIAN F W, et al. 2'-Fucosyllactose alleviate immune checkpoint blockade-associated colitis by reshaping gut microbiota and activating AHR pathway[J]. Food Science and Human Wellness, 2024, 13(5): 2543-2561. DOI:10.26599/FSHW.2022.9250205.

J. Bakshi, K.P. Mishra, Identification of biomarkers for gastrointestinal barrier injury and protective role of sodium butyrate in hypobaric hypoxia exposed rats, Int. Immunopharmacol. 165 (2025) 115424, https://doi.org/10.1016/j.intimp.2025.115424.

M.C. Yu, C.J. Lo, W.C. Lin, W.L. Yen, Y.Y.Hsieh, B.H. Chen, F.S. Lo, Pixel array-based urine biosensor for detection of trimethylamine N-oxide and glucose for early detection of diabetic kidney disease, Anal. Chim. Acta. 1353 (2025) 343951, https://doi.org/10.1016/j.aca.2025.343951.

C. Lan, W. Ren, A. Wu, B. Yu, J. He, Y. Luo, D. Chen, Prevotella copri alleviates diarrhea in weaning piglets through gut microbiota modulation and arachidonic acid-AHR-NRF2 pathway activation, J. Anim. Sci. Biotechnol. 16 (1) (2025) 154, https://doi.org/10.1186/s40104-025-01273-y.

SUN L, WANG T, CHEN B S, et al. Sugarcane leaves-derived polyphenols alleviate metabolic syndrome and modulate gut microbiota of ob/ob mice[J]. Food Science and Human Wellness, 2024, 13(2): 633-648. DOI:10.26599/FSHW.2022.9250048.

J. Jankowski, J. Floege, D. Fliser, M. Böhm, N. Marx, Cardiovascular Disease in Chronic Kidney Disease: Pathophysiological Insights and Therapeutic Options, Circulation. 143 (11) (2021) 1157-1172, https://doi.org/10.1161/CIRCULATIONAHA.120.050686.

Y. Bian, Q. Wang, Q. Liang, Y. Zhu, C. Wu, H. Ruan, X. Hu, Catalpol attenuates postmenopausal osteoporosis by activating SIRT1-mediated P53 deacetylation and inhibiting CASPASE-3-driven osteoblast apoptosis, Int. Immunopharmacol. 168 (Pt 1) (2026) 115820, https://doi.org/10.1016/j.intimp.2025.115820.

X. Lin, S.Q. He, S.K. Shan, F. Xu, F. Wu, F.X. Li, M.H. Zheng, L.M. Lei, J.Y. Duan, Y.Y. Wu, Y.L. Wu, K.X. Tang, R.R. Cui, B. Huang, J.J. Yang, X.B. Liao, J. Liu, L.Q. Yuan, Endothelial cells derived extracellular vesicles promote diabetic arterial calcification via circ_0008362/miR-1251-5p/Runx2 axial, Cardiovasc. Diabetol. 23 (1) (2024) 369, https://doi.org/10.1186/s12933-024-02440-7.